

# Oriented Object Detection in Aerial Images

## Based on Area Ratio of Parallelogram

Xinyi Yu, Mi Lin, Jiangping Lu, Linlin Ou

### Abstract

Rotated object detection is a challenging task in aerial images since the objects in aerial images are displayed in arbitrary directions and are frequently densely packed. Although considerable progress has been made, there are still challenges that existing regression-based rotation detectors suffer from the representation ambiguity. In this paper, we propose a simple, practical framework to optimize the bounding box regression for rotating objects. Rather than directly regressing the five parameters (coordinates of the central point, width, height, and rotation angle) or the four vertices, we employ the area ratio of the parallelogram (ARP) to describe a multi-oriented object accurately. Specifically, ARP regresses coordinates of the center point, height, and width of the oriented object's minimum circumscribed rectangle and three area ratios  $\lambda_1$ ,  $\lambda_2$ , and  $\lambda_3$ . It may facilitate learning offset and avoid the issue of angular periodicity or label points sequence for oriented objects. To further remedy the confusion issue of nearly horizontal objects, the area ratio between the object and its minimal circumscribed rectangle has been used to guide the selection of horizontal or oriented detection for each object. The rotation efficient IOU loss (R-EIOU) connects the flat bounding box with the three area ratios and improves the accuracy of the rotating bounding. Experimental results on remote sensing datasets, including HRSC2016, DOTA, and UCAS-AOD, show that our method achieves superior detection performance than many state-of-the-art approaches. The code and model will be coming with the paper published.

**Keywords:** orientated object detection, aerial image, parallelogram area ratio, rotation efficient IOU loss

## 1. Introduction

Object detection is a vital computer vision technique that aims at classifying and locating the object in images. With the rapid development of satellite remote sensing images and the explosive growth of remote sensing data, object detection in aerial images has been a specific yet activated topic in computer vision [1], [2]. It is widely used in military surveillance, crop monitoring, traffic planning, among other applications. Most traditional methods [3], [4] that rely on manual characteristics to identify objects are sensitive to environmental disruptions like clouds, sunlight, and rain. Although significant progress has been achieved, there is still poor performance, low real-time, and insufficient robustness. Object detection has advanced dramatically in recent years because of deep convolutional neural networks (CNN). Compared with traditional target detection methods, object detection algorithms based on deep learning have the advantages of high accuracy and strong robustness. They are frequently utilized in object detection in remote sensing images.

Object detection can generally be divided into horizontal detection [5], [7], [9], [14] and rotated detection [27], [28], [32], based on the direction of detected boxes. Object detection in aerial images is challenging since the objects have various scales, aspect ratios, and orientations. Moreover, the aerial images contain many objects with dense distributions and extremely unbalanced categories. Consequently, applying the horizontal object detector to aerial images would lead to misalignment

between the detected bounding boxes and ground truth bounding boxes, as shown in Fig. 1(a). The horizontal object detector regresses the horizontal bounding box with four parameters: the abscissa and ordinates of the center point and the length and width of the bounding box. However, the rotated object detector has five parameters. In comparison to the horizontal object detector, the rotating object detector has five parameters and incorporates a regression angle. As illustrated in Fig. 1(b), the rotating detector regresses the smallest circumscribed rectangle of objects, successfully resolving the problem of border misalignment and minimizing the overlapping area of dense objects. Therefore, the oriented object detector is preferred for capturing objects in aerial images.

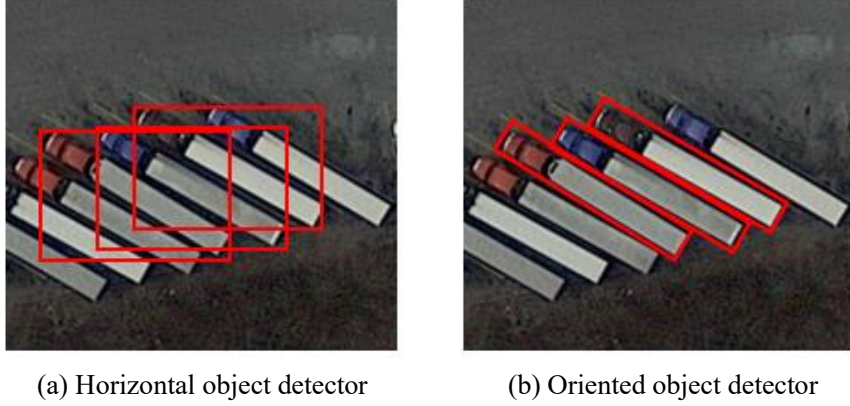


Figure 1: Illustration of horizontal object detector and oriented object detector.

Currently, oriented object detectors characterize spinning objects using five-parameter or eight-parameter regression techniques, introducing representation ambiguity and border discontinuity. **Five-parameter regression methods** [27], [28] adopt  $(x, y, w, h, \theta)$  to represent the rotating objects, which has the issue of periodicity of angle (PoA) and exchangeability of edges (EoE). The underlying problem is that the predicted angle is beyond the defined range. Therefore, the model needs to regress the angle with the complicated form at the boundary, increasing the difficulty of predicting the angle and affecting the model’s performance. This issue is especially pronounced for oriented objects with wide aspect ratios, such as harbors and bridges in aerial photos, as well as long text lines in scene images. **Eight-parameter regression methods** [31] typically utilize four vertices to represent the rotating objects, which creates ambiguity when defining the bounding box order of the four vertices. Theoretically, there are 24 different representations for a single bounding box, so it also faces the problem of border discontinuity. As a result, whether employing five-parameter or eight-parameter regression, an object might be represented in various ways, complicating the regression process and degrading detection performance further.

Recently, several approaches have been proposed, such as **BBAVectors** [33], **Gliding vertex** [32], **P-RSDet** [38], **IOU-Smooth L1 loss** [30], **Modulated Loss** [31], **RIL** [36], **GWD** [37]. They are, however, regression-based detection approaches, and the underlying boundary problem has not been solved. **SCL** [34] and **DCL** [35] are novel approaches to solving boundary issues. The prediction of the object angle is transformed into a classification problem with the goal of limiting the forecast result to a specified range. Nevertheless, they lost some accuracy and increased the amount of calculation. Without a unified solution, these concerns would continue to exist and will have a significant impact on detection performance, particularly at the boundary position.

This article suggests a straightforward yet effective solution called the Area Ratio of Parallelogram

(ARP), which has a single representation form and applies to the boundary problem in aerial photos and scene text. To characterize the rotating object precisely, we use the center point coordinates, the width and height of the directed object’s minimal bounding rectangle, and the three area ratio. The three area ratios are as follows: one is the area ratio of the rotating target to the smallest boundary rectangle. At the same time, the other two are the area ratios of the two parallelograms and the rotating object’s smallest bounding rectangle (will be explained in section 3.2). Empirically, this approach is superior to forecast five-parameter or eight-parameter bounding boxes directly. To exacerbate the problem of almost horizontal objects confusing, we use the area ratio between the object and its minimum circumscribed rectangle to determine whether to detect the object horizontally or oriented. Smooth L1 loss assumes that each point within the detection box is independent, but there is some correlation between them. However, IOU loss, DIOU loss, CIOU loss, and EIOU loss are not differentiable in object-oriented detection. As a result, we suggest a rotation focal and efficient IOU loss (R-EIOU) to handle the undifferentiable problem and enhance the accuracy of the rotating bounding box. In summary, the main contributions of this paper are:

1. The orientated bounding box can be described using the area ratio of a parallelogram (ARP). It is straightforward yet effective in resolving the problem of boundary loss. ARP outperforms the baseline technique in recognizing rotated objects, which relies on regression to estimate the center point coordinates, height, breadth, and angle of oriented objects.
2. The obliquity factor is the area ratio of the orientated object to its smallest circumscribed rectangle. It effectively selects horizontal detection for nearly horizontal objects and oriented detection for others, resolving the confusing issue.
3. As an alternative to the smooth L1 loss, we propose a novel loss function called R-EIOU. It successfully solves the boundary problem of orientated bounding box regression and achieves higher accuracy in rotated detection when compared to the smooth L1 loss.
4. Experiments show that our method can be easily embedded in different backbones and significantly improve the performance in oriented object detection. It achieves superior performance on four public datasets and three popular detectors.

## 2. Related Work

### 2.1 Horizontal Object Detection

In recent years, object detection has advanced significantly and can be roughly classified into two categories: two-stage detectors and one-stage detectors. The two-stage detectors first generate a series of regions of interest (RoIs) and then use the features of the regions to predict the object categories and regress the bounding boxes. Numerous high-performance two-stage detectors have been developed, such as [R-CNN \[5\]](#), [Fast R-CNN \[6\]](#), [Faster R-CNN \[7\]](#), [Mask R-CNN \[8\]](#). Although two-stage approaches have shown promising results on some benchmarks, one-stage detectors simplify the detection process by treating it as a regression problem and achieving higher speed. [YOLO \[9\]](#) and its variances ([YOLO9000 \[10\]](#), [YOLOv3 \[11\]](#), [YOLOv4 \[12\]](#), [YOLOv5](#)), [SSD \[13\]](#), and [RetinaNet \[14\]](#) are representative single-stage approaches. Compared with anchor-based methods, various anchor-free techniques, such as [Cornernet \[15\]](#) and [CenterNet \[16\]](#), have exploded in popularity in recent years, opening up a new direction for object detection. Loss function plays a critical role in object detection. It has a significant impact on object detection performance and continues to improve with the advancement of target detectors. Since [Smooth L1 loss \[17\]](#) is robust and resistant to outliers, it is commonly utilized in Fast R-CNN and Faster R-CNN. This approach

assumes the four points of the bounding box are independent, whereas they are actually connected. It has been demonstrated that the use of **IoU-induced loss**[18], such as **GIOU**[19], **DIOU**[20], and **Focal-EIOU**[21], can assure the consistency of the final detection metric and loss in conventional horizontal detectors. However, these IoU losses cannot be used directly in rotation detection due to the indifferentiability of the rotating IoU.

The above detectors generate bounding boxes solely in the horizontal direction, which frequently mismatch the objects in aerial photos due to the arbitrarily rotated and densely distributed objects in remote sensing images. As a result, the recognition of rotatable objects has become a prominent direction in aerial photos and scene text.

## 2.2 Rotated Object Detection

Typically, rotated object detectors use oriented bounding boxes to describe the positions of objects, which eliminates the issue of misalignment and is excellent for capturing objects in aerial images and scene text. Numerous effective detectors for scene text detection have been proposed, including **R<sup>2</sup>CNN** [22], **RRPN** [23], **TextBoxes++** [24], **RRD** [25], **EAST** [26]. These approaches are generally extended from horizontal object detectors by including an angle and some measures to adapt the detection of objects in scene text. However, object detection is more challenging in aerial photos since the objects are frequently small, numerous, and scattered with large-scale changes. It is hard to demonstrate promising performance in remote sensing images using the excellent methods described above. Hence, many robust rotated object detectors have emerged in aerial images. For example, **RoI transformer** [27] suggests **RRoI Leaner** and **RRoI Warping**. **RRoI Leaner** transforms horizontal RoIs into rotated RoIs, and **RRoI Wrapping** extracts the rotation-invariant feature from the oriented RoI for subsequent object classification and location regression. **R<sup>3</sup>Det** [28] is a one-stage rotation detector based on **RetinaNet** that solves the feature misalignment problem by employing cascade regression and refining the bounding box. **CFC-Net** [29] designs a **Polarized Attention Module (PAM)**, refines the preset horizontal anchor points, and adopts **Dynamic Anchor Learning (DAL)** strategy to achieve high performance in rotating object detection. While the preceding solutions are promising, they overlook the issue of the discontinuous border. It will result in a discontinuous regression loss and will impede the convergence of network training. Thus, multiple rotational object detectors have been developed, each of which attempts to overcome the obstacles mentioned above in a unique way. For instance, **SCRDet** [30] and **RSDet** [31] propose **IOU-smooth L1 loss** and **modulated loss** to alleviate the sharp increase loss caused by the angular periodicity, allowing for improved handling of small, clutter, and rotated objects. **Gliding Vertex** [32] glides the vertex of the horizontal bounding box to represent a rotatable object, alleviating the issue of border discontinuity and achieving more precise object detection. **BBAVectors** [33] presents a **box boundary-aware bounding box description**. The **BBAVectors** are distributed in the four quadrants of the Cartesian coordinate system, which is superior to directly forecasting the spatial characteristics of bounding boxes. **CSL** [34] and **DCL** [35] regard angular prediction as a classification task to avoid the discontinuity of regression loss.

**RIL** [36] optimizes the bounding box regression for the rotating objects through **Representation Invariance Loss**, which solves the inconsistency between the loss and localization quality caused by ambiguous representations. **GWD** [37] introduces the **Gaussian Wasserstein Distance Loss** to approximate the non-differentiable rotation IOU-induced loss, which can elegantly resolve border discontinuity and square-like problems.

In summary, all of the solutions above turn definitions of rotating objects or create more precise loss functions to handle the border discontinuity problem. Nonetheless, there is no fully unified answer to all of the issues above. In order to increase the performance and speed in aerial images and scene text, we provide the ARP to describe a rotating object and create an R-EIOU loss to approximate the non-differentiable rotation IOU.

### 3. Proposed Method

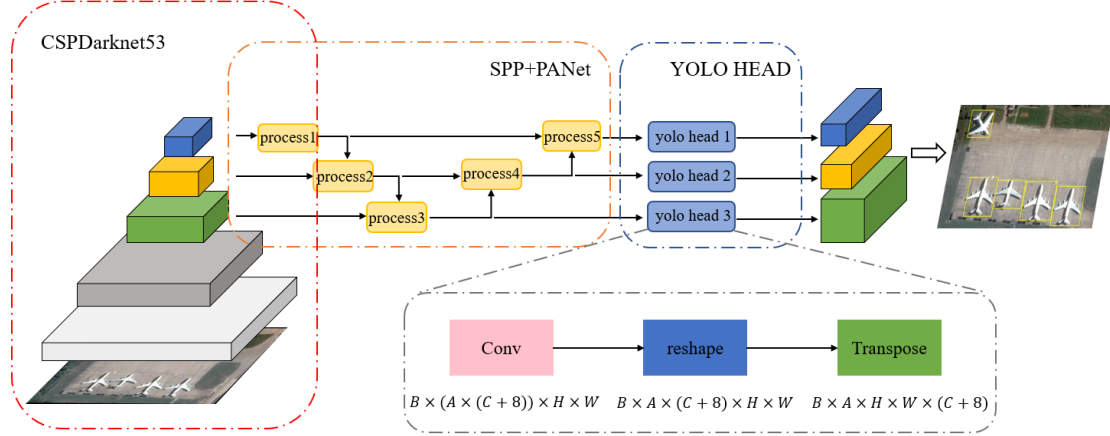


**Figure 2:** Network architecture of proposed rotation detector (YOLOv5 as an embodiment). CSPDarknet53, SPP+PANet, and YOLO HEAD are the primary components of the proposed detector. We add three extra object variables  $(\lambda_1, \lambda_2, \lambda_3)$  to the head of YOLOv5. The symbols ‘H’ and ‘W’ refer to the length and width of the grid, and ‘B’ is the batch size of the sample. ‘C’ and ‘A’ represent the number of categories and predefined anchors, respectively, while ‘8’ denotes the confidence and representation method  $(x, y, w, h, \lambda_1, \lambda_2, \lambda_3)$ .

In this section, we will expound on the suggested method in the order listed below. First, the general architecture of our technique is depicted in Fig. 2. A single-stage rotation detector based on YOLOv5 is used in this embodiment. Then, we adopt the area of the parallelogram (ARP) to describe rotating objects accurately, which has a unique representation. Specifically, the directed object is regressed using its center point coordinates, the width and height of its smallest bounding rectangle, and the three area ratios. It is easier to learn the orientation and scale information of the object, effectively solving the problem of boundary discontinuity. Additionally, the area ratio between the rotating object and its minimum circumscribed rectangle is also used as an obliquity factor for selecting the oriented or horizontal bounding boxes. At last, to more correctly express loss in oriented object identification, the R-EIOU has been proposed.

#### 3.1 Network Architecture

YOLOv5 is one of the most advanced single-stage object detectors. We extend YOLOv5 to the oriented object detection to prove the effectiveness of ARP. Its network architecture is sketched in Fig. 2. Append three additional object variables  $(\lambda_1, \lambda_2, \lambda_3)$  to the head of YOLOv5 and alter its loss function to favor orientated object recognition. Specifically, we first use the CSPDarknet53 [12] as the backbone to extract deep features and generate bounding. Then the features are fused and extracted by SPP and PANet. Finally, the direction box’s category, confidence, and parameters are produced via YOLO HEAD, including a horizontal bounding box  $(x, y, w, h)$ , as well as three area

ratios  $(\lambda_1, \lambda_2, \lambda_3)$ . Additionally, the area ratio  $\lambda_1$  between the rotating object and its smallest circumscribed rectangle is employed to determine the obliquity of the orientated or horizontal bounding boxes. If the obliquity factor  $\lambda_1$  of each candidate is more than a threshold, suggesting that the underlying object is roughly horizontal, the horizontal bounding box is chosen as the final detection. Otherwise, oriented bounding is used as the final detection method.

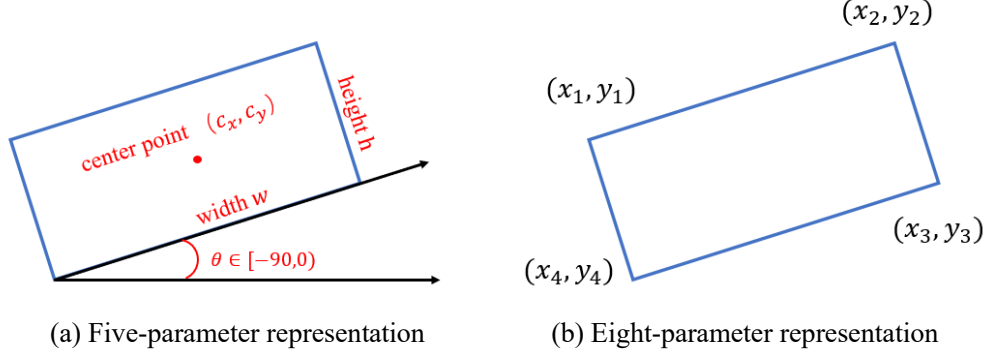


Figure 3: Common representation method for oriented object detection

### 3.2 ARP Representation Method

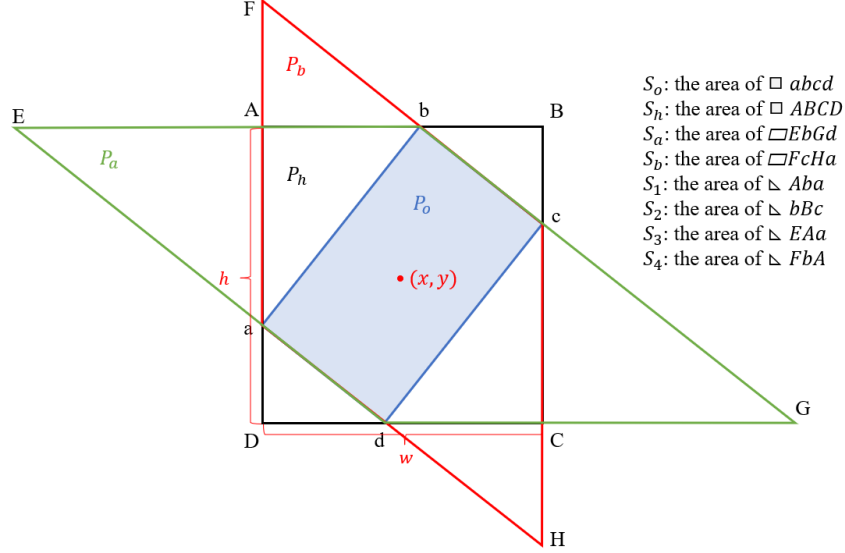
**Representation Method:** Most current object detection systems use five-parameter or eight-parameter regression techniques to describe rotating objects. As illustrated in Fig. 3(a), the five-parameter formulation is consistent with that of OpenCV, which uses the center point coordinates  $(c_x, c_y)$ , width  $w$ , height  $h$ , and angle  $\theta$  of the oriented boxes to describe spinning objects. While a tiny angle variation has a negligible effect on the total loss during training, it can result in a substantial IOU disparity between the predicted and ground-truth boxes. As a result, boundary regression will exhibit inconsistencies. As demonstrated in Fig. 3(b), the eight-parameter method typically uses four boundary points  $(x_1, y_1, x_2, y_2, x_3, y_3, x_4, y_4)$  to represent the spinning object. The sequence of the four corner points, on the other hand, introduces inconsistencies in the model’s regression process. Thus, whether the five-parameter or eight-parameter regression is applied, border discontinuities will arise.

This paper introduces a simple representation for oriented objects and a novel detection scheme that divides and conquers nearly horizontal and oriented object detection. To be more specific, we offer the Area Ratio of Parallelogram (ARP) approach for precisely describing an oriented object parameterized by seven tuples  $(x, y, w, h, \lambda_1, \lambda_2, \lambda_3)$ , as illustrated in Fig. 4. For every rotating object  $P_o$  (see the blue box in Fig. 4), its left, upper, right, and bottom vertices are represented by  $(a, b, c, d)$ . The black box in Fig. 4 represents the oriented object’s smallest circumscribed rectangle  $P_h$ , and its four vertices rectangle are denoted by  $(A, B, C, D)$ .  $(x, y, w, h)$  denotes the center point, width, and height of the minimal bounding rectangle of the rotating object  $P_h$ .  $\lambda_1$  is the area ratio between the oriented object  $P_o$  and minimum circumscribed rectangle  $P_h$ .  $\lambda_2$  is the area ratio of the parallelogram  $P_a$  (see the green box in Fig. 4) to the smallest circumscribed rectangle  $P_h$ . The parallelogram  $P_a$  is formed by the extension line of the right side of the oriented object’s top vertex and the extension line of the width of the smallest circumscribed rectangle.  $\lambda_3$  is the area ratio of the parallelogram  $P_b$  (represented by the red box in Fig.4) to the smallest circumscribed rectangle  $P_h$ . The parallelogram  $P_b$  comprises the extension line of the right side of the top vertex on the

oriented object and the extension line of the height of the smallest circumscribed rectangle. The parameter  $\lambda_1$ ,  $\lambda_2$  and  $\lambda_3$  are defined as follows:

$$\begin{cases} \lambda_1 = S_o/S_h \\ \lambda_2 = S_a/S_h \\ \lambda_3 = S_b/S_h \end{cases} \quad (1)$$

where  $S_o$ ,  $S_h$ ,  $S_a$ , and  $S_b$  are the areas of the oriented object, minimum circumscribed rectangle, and two parallelograms, respectively.



Oriented bounding box:  $(x, y, w, h, \lambda_1, \lambda_2, \lambda_3)$

**Figure 4:** Illustration of ARP representation method. Rectangles coloured in blue, black, green, and red represent the oriented object  $P_o$ , the minimum circumscribed rectangle  $P_h$  and two parallelograms  $P_a$ ,  $P_b$ , respectively, and their areas are  $S_o$ ,  $S_h$ ,  $S_a$  and  $S_b$ . We adopt  $(x, y, w, h, \lambda_1, \lambda_2, \lambda_3)$  to represent oriented objects.

**Solve Side Lengths and Vertex Coordinates:** According to the ARP representation method in **Fig.4**, the area of the rotating object, the minimum circumscribed, and two parallelograms can be obtained as follows:

$$\begin{cases} S_h = S_o + 2(S_1 + S_2) \\ S_a = S_o + 2(S_1 + S_3) \\ S_b = S_o + 2(S_1 + S_4) \end{cases} \quad (2)$$

where  $S_1$ ,  $S_2$ ,  $S_3$ , and  $S_4$  denote the areas of triangles  $\triangle Aba$ ,  $\triangle bBc$ ,  $\triangle EAa$ , and  $\triangle FbA$ , respectively. Since the oriented object in aerial images is denoted by a rectangular box, and its smallest circumscribed rectangle is also a rectangle box, our represent method contains two pairs of similar triangles  $\triangle EAa \sim \triangle EAa$  and  $\triangle EAa \sim \triangle EAa$ . Given their similarity ratios of  $k_1$  and  $k_2$ , respectively. We can derive the following relationships between the four triangles:

$$\begin{cases} S_3/S_2 = k_1^2 \\ S_4/S_2 = k_2^2 \\ S_1/S_2 = k_1k_2 \end{cases} \quad (3)$$

Combine **Eqs. (2)** and **(3)**, the values of  $k_1$  and  $k_2$  can be obtained as follows:

$$\begin{cases} k_1 = \sqrt{\frac{(S_a - S_o)^2}{(S_h - S_o)(S_a - S_o) + (S_h - S_a)(S_b - S_o)}} \\ k_2 = \sqrt{\frac{(S_b - S_o)^2}{(S_h - S_o)(S_a - S_o) + (S_h - S_a)(S_b - S_o)}} \end{cases} \quad (4)$$

By substituting Eq. (4) into Eq. (1), yields  $k_1$  and  $k_2$ .

$$\begin{cases} k_1 = \sqrt{\frac{(\lambda_2 - \lambda_1)^2}{(1 - \lambda_1)(\lambda_2 - \lambda_1) + (1 - \lambda_2)(\lambda_3 - \lambda_1)}} \\ k_2 = \sqrt{\frac{(\lambda_3 - \lambda_1)^2}{(1 - \lambda_1)(\lambda_2 - \lambda_1) + (1 - \lambda_2)(\lambda_3 - \lambda_1)}} \end{cases} \quad (5)$$

Additionally, the length and coordinates of the rotating object's intersection point with its smallest circumscribed rectangle can also be obtained as follows:

$$\begin{cases} h_1 = |Aa| = \frac{k_1}{1+k_1} h \\ h_2 = |aD| = \frac{1}{1+k_1} h \\ w_1 = |Ab| = \frac{k_2}{1+k_2} w \\ w_2 = |bB| = \frac{1}{1+k_2} w \end{cases} \quad (6)$$

$$\begin{cases} a: (x - w/2, y - h/2 + h_1) \\ b: (x - w/2 + w_1, y - h/2) \\ c: (x + w/2, y + h/2 - h_1) \\ d: (x + w/2 - w_1, y + h/2) \end{cases} \quad (7)$$

where  $h_1, h_2$  denote the length of line segment Aa and aD, and  $w_1, w_2$  indicate the length of the Ab and bB line segment.  $(a, b, c, d)$  represent the coordinates of the four vertices of the oriented object.

It is seen that the ARP representation method can accurately describe the position information of the rotating object in the image. We can convert the ARP to the more common eight-parameter representation method by applying the Eqs. (5), (6), and (7). Similarly, converting the eight-parameter representation method to our representation method is straightforward. Thus, our method of representation accurately describes rotating objects and has a unique representation. It solves the discontinuous boundary problem effectively and significantly improves the detection accuracy of rotating objects.

**Nearly Horizontal Bounding Box:** In practice, we observe that the detection fails when an object extremely approaches the horizontal bounding box, as illustrated in Fig. 5. When the oriented object is close to the horizontal bounding box, the parameter  $\lambda_1$  and one of the parameters in  $\lambda_2$  and  $\lambda_3$  approach one infinitely. Thus, it will be impossible to obtain the rotating object's four vertex coordinates since the value of the parameter  $k_1$  or  $k_2$  is infinite (calculated by Eq. (5)). We regard this problem as an extreme case. To address this case, we divide the rotating objects into oriented bounding boxes (OBBs) and horizontal bounding boxes (HBBs) and process them independently in this work. The advantage of this classification strategy is that it allows us to convert difficult-to-handle corner cases into HBBs cases. A nearly horizontal object has a high area ratio  $\lambda_1$  that is close to one (see Fig. 5), whereas a highly slender oriented object has a low area ratio  $\lambda_1$  that is close to zero. Therefore, we adopt the area ratio  $\lambda_1$  as an obliquity factor to guide the selection of OBB and HBB. Without introducing other parameters, the categories of OBB and HBB can be finished. Indeed, it is reasonable to represent nearly horizontal objects with horizontal bounding

boxes.

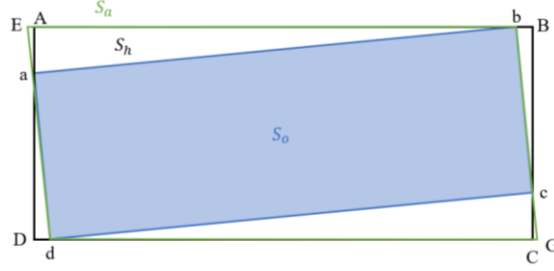


**Figure 5: Illustration of the nearly horizontal bounding box cases.** The object box  $S_o$ , the minimum circumscribed rectangle  $S_h$  and parallelogram  $S_a$  are nearly equal in area.

### 3.3 R-EIOU Loss

The proposed method is based on YOLOv5. Thus the loss function makes some appropriate modifications based on YOLOv5. The multi-task loss is defined as follows:

$$L = \lambda_{box} \sum_{i=0}^{K \times K} \sum_{j=0}^M I_{ij}^{obj} L_{box} + \lambda_{obj} \sum_{i=0}^{K \times K} \sum_{j=0}^M I_{ij}^{obj} L_{obj} + \lambda_{cls} \sum_{i=0}^{K \times K} I_{ij}^{obj} \sum_{c \in cls} L_{cls} + \lambda_{\alpha} \sum_{i=0}^{K \times K} \sum_{j=0}^M I_{ij}^{obj} L_{\alpha} \quad (8)$$

where  $K \times K$  denotes the number of grids,  $M$  indicates the number of candidate boxes produced by each grid. Each candidate box will get a corresponding bounding box through the network, so we finally obtain the  $K \times K \times M$  bounding boxes.  $I_{ij}^{obj}$  is a binary label that indicates whether the  $j$  anchor box of the  $i$  grid is responsible for detecting this object. If it is responsible, it is set to 1; otherwise, it is set to 0. The hyper-parameters  $\lambda_{obj}$ ,  $\lambda_{cls}$ ,  $\lambda_{box}$ , and  $\lambda_{\alpha}$  are used to balance the importance of each loss term. The confidence loss  $L_{obj}$  and classification loss  $L_{cls}$  are both Focal loss, which are the same as that in YOLOv5.  $L_{box}$  signifies the loss for bounding box regression.  $L_{\alpha}$  denotes the loss for obliquity factor  $\lambda_1$  regression, which is defined as the binary cross-entropy:

$$L_{cls} = -(\alpha \cdot \log(p(\alpha)) + (1 - \alpha) \log(1 - p(\alpha))) \quad (9)$$

where  $\alpha$  denotes a binary label of either 0 or 1,  $p(\alpha)$  represents the probability that the output corresponds to the  $\alpha$  label. The following is the definition of  $\alpha$ :

$$\alpha = \begin{cases} 1 (OBB) & \lambda_1 < \lambda_{thr} \\ 0 (HBB) & otherwise \end{cases} \quad (10)$$

where  $\lambda_{thr}$  is the threshold used to differentiate between the oriented and horizontal bounding boxes, and its optimal value will be determined in [Chapter 4](#). The loss function for the  $L_{box}$  regression contains two terms for the horizontal bounding box  $(x, y, w, h)$  and three area ratios  $(\lambda_1, \lambda_2, \lambda_3)$ . In terms of the horizontal bounding box,  $L_{box}$  is the same as the CIOU loss in YOLOv5. Compared with the horizontal bounding, the oriented bounding box adds three parameters  $\lambda_1, \lambda_2, \lambda_3$  in the head. Therefore, it needs to augment extra loss to calculate these three variables and facilitate their regression. Smooth L1 loss is a relatively good loss function for rotating object detection because it can promote object regression without introducing the non-derivation problem. Smooth L1 loss is a relatively excellent loss function in rotating object detection, which can promote the regression of the target without the problem of non-differentiable. Therefore, we also considered using Smooth L1 loss to initially deal with the parameters of these three area ratios. Given a

predicted horizontal bounding box  $B$  and a target horizontal bounding box  $\hat{B}$ , their losses are defined as follows:

$$L_{box} = L_{CIoU} + \sum_{l=1}^3 \text{smoothL1}(\lambda_l - \hat{\lambda}_l) \quad (11)$$

where  $L_{CIoU}$  denotes the CIOU loss between the two horizontal boxes  $B$  and  $\hat{B}$ . Furthermore, three area ratios calculate the additional area ratio loss using Smooth L1 loss.

In practice, we observe that using only CIOU to address horizontal bounding and Smooth L1 loss to address three area ratios generates boundary problems in the case of nearly horizontal bounding boxes. As demonstrated in Fig. 6(a), some bounding boxes do not correspond to the objects when Smooth L1 loss is applied. Therefore, we propose R-EIOU loss to better solve this problem. Given two predicted parallelogram boxes  $P_a$  and  $P_b$  (see Fig. 4) and two target boxes  $\hat{P}_a$  and  $\hat{P}_b$ , the R-EIOU loss is defined as follows:

$$L_{box} = 1 - IoU + \frac{\rho^2(b, \hat{b})}{c^2} + \frac{\rho^2(w_{pa}, \hat{w}_{pa})}{c_{wpa}^2} + \frac{\rho^2(h_{pb} + \hat{h}_{pb})}{c_{hpb}^2} \quad (12)$$

where  $IoU$  represent the Intersection over Union between the  $B$  and  $\hat{B}$ .  $b$  and  $\hat{b}$  denote the central points of  $B$  and  $\hat{B}$ , respectively.  $\rho(\cdot) = \|\cdot\|$  indicates the Euclidean distance. The diagonal length of the smallest enclosing box that encompasses the two horizontal bounding boxes  $B$  and  $\hat{B}$  is denoted by  $c$ .  $w_{pa}$  and  $\hat{w}_{pa}$  signify the width of  $P_a$  and  $\hat{P}_a$ , respectively.  $c_{wpa}$  is the width of the smallest enclosing box covering the two parallelogram boxes  $P_a$  and  $\hat{P}_a$ .  $h_{pb}$  and  $\hat{h}_{pb}$  denote the height of  $P_b$  and  $\hat{P}_b$ , respectively. The height of the smallest enclosing box covering the two parallelogram boxes  $P_b$  and  $\hat{P}_b$  is denoted by  $c_{hpb}$ . Namely, we divide the loss function into three parts: the IOU loss  $1 - IoU$ , the distance loss  $\rho^2(b, \hat{b})/c^2$ , and the area ratio loss  $\rho^2(w_{pa}, \hat{w}_{pa})/c_{wpa}^2 + \rho^2(h_{pb}, \hat{h}_{pb})/c_{hpb}^2$ . The R-EIOU loss effectively solves the problem of inaccurate expression of box regression loss function, especially in the case of an approximate horizontal bounding box (see Fig. 6(b)). Experiments show that the detector based on this R-EIOU loss can achieve more considerable gains than Smooth L1 loss.



(a) Smooth L1 loss

(b) R-EIOU loss

Figure 6: Comparison of detection results by two losses.

## 4. Experiments

Experiments are performed with Pytorch on a server with 8 GeForce RTX 2080 Ti and  $11 \times 8G$  memory. We first give the description of the dataset and then use these datasets to verify the advantage of the proposed method.

### 4.1 Datasets and Implementation Details

**DOTA [1]:** DOTA is a large-scale benchmark and challenge for object detection in aerial images, and it is currently the most comprehensive remote sensing image data set for object detection. There

are three versions of this data set that has been released, including DOTAv1.0, DOTAv1.5, and DOTAv2.0. Since the current rotation object detection algorithms are based on DOTAv1.0, the experiment in this paper is mainly completed on DOTAv1.0 to verify the performance of our proposed method. DOTAv1.0 includes 2,806 aerial images with 188,282 annotated instances, and the size of the image ranges from around  $800 \times 800$  to  $4,000 \times 4,000$  pixels. There are 15 categories in total, including plane (PL), baseball diamond (BD), bridge (BR), ground track field (GTF), small vehicle (SV), large vehicle (LV), ship (SH), tennis court (TC), basketball court (BC), storage tank (ST), soccer ball field (SBF), roundabout (RA), harbor (HA), swimming pool (SP) and helicopter (HC). It uses 1/2 of the images as the training set, 1/6 as the verification set, and 1/3 as the test set. The test set results are not public, and it needs to be uploaded to the server for test. Due to the ariel images have different sizes, we divide the images into  $1,024 \times 1,024$  pixel sub-images with an overlap of 200 pixels, with is the same as [RoI Transformer \[27\]](#). We obtain 10,948 training images, 3,568 verification images, and 10,019 test images with all these processes.

**HRSC2016 [2]:** The HRSC2016 is a challenging dataset for ship detection in aerial images. All images come from six famous ports, including two scenes of marine vessels and offshore vessels. It contains 1,061 images and more than 20 categories of ships in various appearances. The image size ranges from  $300 \times 300$  to  $1500 \times 900$ . The training, validation and test sets contain 436 images (including 1,207 instances), 181 images (including 541 instances) and 444 images (including 1,228 instances).

**UCAS-AOD [39]:** USCA-AOD is a remote sensing data set for the detection of vehicles and planes issued by the University of Chinese Academy of Sciences. It contains 1,510 aerial images of approximately  $659 \times 1,280$  pixels, with two categories of 14,596 instances in total. In line with [ICN \[41\]](#) and [DOTA \[1\]](#), we randomly select 1,110 images for training and 400 images for testing.

**ICDAR2015 [40]:** ICDAR2015 is a data set for scene text detection and location proposed by ICDAR 2015 Robust Reading Competition. It contains a total of 1,500 images, of which 1,000 are utilized for training and the remainder for testing. Four vertices of the quadrangle annotate the text regions.

**Baseline and Training Details:** To demonstrate the generality of our system, we conduct experiments on three aerial benchmarks and one scene text benchmark. We adopt [RetinaNet \[14\]](#), [R<sup>3</sup>Det \[28\]](#), and YOLOv5 as the baseline in all ablation studies and adopt YOLOv5 as final experiments. The initial learning rates for RetinaNet, R<sup>3</sup>Det, and YOLOv5 are 0.0005, 0.001, and 0.01, respectively. The momentum and weight decay are 0.9 and 0.0001, respectively. **The baseline of our experiment is YOLOv5 unless otherwise specified.** The training epoch for DOTAv1.0, HRSC2016, USAS-AOD, and ICDAR2015 are 300, 200, 150, and 150, respectively. Additionally, the number of iterations of each epoch is proportional to the sample size in the dataset. The warm-up approach is used to determine an appropriate learning rate during the first quarter of the training epochs. The final detection results are post-processed using rotating non-maximum suppression (R-NMS) during the inference. The hyperparameters  $\lambda_{box}$ ,  $\lambda_{cls}$ ,  $\lambda_{obj}$  and  $\lambda_{\alpha}$  in [Eq. \(4\)](#) are set to 0.05, 0.3, 0.7 and 0.8, respectively. Without the extra declaration, other hyper-parameter settings related to the program are consistent with YOLOv5.

## 4.2 Ablation Study

In this section, we conduct a series of ablation experiments on DOTA-v1.0, HRSC2016, UCAS-AOD, and ICDAR2015 datasets to evaluate the effectiveness of our proposed method. For fair

compassion, all baseline methods are implemented using similar settings to the proposed method. Please take note that we do not employ sophisticated data augmentation techniques in this section.

#### 4.2.1 Evaluation of ARP Representation Method

We employ the RetinaNet, R<sup>3</sup>Det, and YOLOv5 as our baseline to evaluate the effectiveness of the ARP representation method. Notably, the baseline method shares the same architecture and loss (Smooth L1 loss) as the proposed method except for the output box representations. We compare our ARP method to others that employ different representations, as illustrated in Tab. 1. The suggested method outperforms OpenCV representation (DOC) on RetinaNet, R3Det, and YOLOv5 by 3.03%, 0.96%, and 1.71%, respectively, on the DOTAv1.0 dataset. Additionally, we conduct comparative tests on the HRSC2016 dataset to confirm the boosting effect of ARP. Results show that our ARP method also achieves predominant performance. The result suggests that the ARP representation approach is superior to learning the five-parameter (DOC and DLE [37]) and angle classification methods (CSL [34] and DCL [35]) for detecting orientated objects.

**Table 1:** Ablation study for ARP on three baselines. Where DOC denotes the defined method based on OpenCV, DLE indicates the defined method based on the long edge.

method	backbone	datasets	BOX DEF	mAP
RetinaNet	Resnet50	DOTAv1.0	DLE	64.17
			DOC	65.73
			CSL	67.38
			DCL	67.39
			<b>ARP (ours)</b>	<b>68.76</b>
		HRSC2016	DOC	84.28
		<b>ARP (ours)</b>	<b>86.43</b>	
R <sup>3</sup> Det	Resnet50	DOTAv1.0	DOC	70.66
			DCL	71.21
			<b>ARP (ours)</b>	<b>71.62</b>
		HRSC2016	DOC	88.52
		<b>ARP (ours)</b>	<b>88.93</b>	
YOLOv5	CSPDarknet53 (yolov5x)	DOTAv1.0	DOC	71.12
			<b>ARP (ours)</b>	<b>72.83</b>
		HRSC2016	DOC	88.65
			<b>ARP (ours)</b>	<b>89.07</b>

#### 4.2.2 Evaluation R-EIOU Loss

We construct R-EIOU loss for our ARP approach, as indicated in Section 3.4. As illustrated in Tab.2, we utilize four distinct datasets to test the effectiveness of the R-EIOU loss. As mentioned previously, the basic model is YOLOv5. The regression head produces the orientated bounding box, which is represented by four bounding box parameters and three area ratios. R-EIOU loss achieves mAP values of 73.33%, 89.46%, 96.58%, and 84.43% on the DOTAv1.0, HRSC2016, USAS-AOD, and ICDIR2015, respectively, which is an improvement of 0.50%, 0.39%, 0.42%, and 0.27% over the baseline model. R-EIOU loss of the orientated bounding box combines horizontal bounding box and area ratio, resolving boundary difficulties and promoting network convergence. Thus, the R-EIOU loss design is effective for our ARP approach.

Table 2: Ablation study for R-EIOU loss on three datasets.

method	backbone	datasets	Loss	mAP
YOLOv5	CSPDarknet53 (yolov5x)	DOTAv1.0	Smooth L1 loss	72.83
			<b>R-EIOU loss</b>	<b>73.33</b>
		HRSC2016	Smooth L1 loss	89.07
			<b>R-EIOU loss</b>	<b>89.46</b>
		UCAS-AOD	Smooth L1 loss	96.16
			<b>R-EIOU loss</b>	<b>96.58</b>
		ICDAR2015	Smooth L1 loss	84.16
			<b>R-EIOU loss</b>	<b>84.43</b>

### 4.2.3 Hyperparameters of ARP

We undertake parameter sensitivity tests to determine the optimal hyperparameter settings. As discussed in Section 3.2, ARP regression is accurate for oriented objects but less accurate for objects close to the level due to the possibility of confusion. YOLOv5 is used as a baseline to examine the influence of various obliquity factor thresholds  $\lambda_{thr}$  on four datasets. As depicted in Fig. 7, the best thresholds in DOTAv1.0, HRSC2016, USAS-AOD and ICDIR2015 are 0.94 (0.95), 0.92, 0.96 and 0.91 (0.92), respectively. Indeed, when a low threshold is used, horizontal bounding boxes are used to represent some oriented objects, resulting in lower oriented object identification performance. However, almost horizontal objects may have difficulty discriminating between horizontal and orientated bounding boxes when a wide threshold is used. Therefore, it is vital for us to choose appropriate threshold values across distinct datasets.

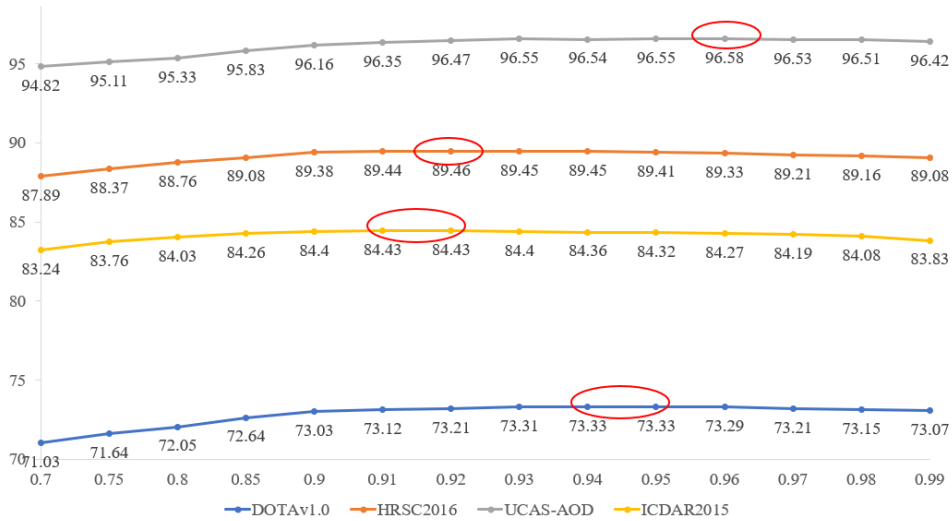


Figure 7: Ablation study on four datasets with varying obliquity thresholds  $\lambda_{thr}$ .

### 4.3 Comprehensive Overall Comparison

We compare our proposed technique to other state-of-the-art methods in this part using three aerial image detection datasets, DOTA, HRSC2016, and UCAS-AOD, as well as one scene text detection dataset, ICDAR2015.

### 4.3.1 Results on DOTA

On DOTA datasets, we compare the proposed technique to various outstanding detectors, as depicted in Tab. 3. Because the test set’s ground-truth labels are not publicly available, the detection results should be submitted to the official DOTA assessment site. Our approach achieves 75.31% and 76.05% mAP, respectively, using YOLOv5x and YOLOv5x6 as the backbone. Moreover, As can be observed, introducing R-EIOU improves performance by 1.69% and results in 77.74% mAP. In addition, it achieves 79.93% mAP with YOLOv5x6 in the multi-scale (0.5, 1.0, 1.5, 2.0) during training and testing. The experimental evidence indicates that our method outperforms previous methods, particularly for objects with dense packing and many directions (see SV, LV, SH, and TC in Tab. 3). Fig. 8 illustrates some DOTA dataset results.

**Table 3:** Performance evaluation of OBB task on DOTAv1.0 dataset. R-101 indicates ResNet-101(likewise for R-50), and H-104 stands for Hourglass-104. YOLOv5x and YOLOv5x6 denote different models in YOLOv5. \* denotes multi-scale training and testing.

methods	backbone	PL	BD	BR	GTF	SV	LV	SH	TC	BC	ST	SBF	RA	HA	SP	HC	mAP
Two-stage:																	
RRPN[23]	R-101	88.52	71.20	31.66	59.30	51.85	56.19	57.25	90.81	72.84	67.38	56.69	52.84	53.08	51.94	53.58	61.01
ICN[41]	R-101	81.36	74.30	47.70	70.32	64.89	67.82	69.98	90.76	79.06	78.20	53.64	62.90	67.02	64.17	50.23	68.16
RoI Trans.[28]	R-101	88.64	78.52	43.44	75.92	68.81	73.68	83.59	90.74	77.27	81.46	58.39	53.54	62.83	58.93	47.67	69.56
CAD-Net[42]	R-101	87.80	82.40	49.40	73.50	71.10	63.50	76.70	90.90	79.20	73.30	48.40	60.90	62.00	67.00	62.20	69.90
SCRDet[30]	R-101	89.98	80.65	52.09	68.36	68.36	60.32	72.41	90.85	87.94	86.86	65.02	66.68	66.25	68.24	65.21	72.61
Gliding Vet.[33]	R-101	89.64	85.00	52.26	77.34	73.01	73.14	86.82	90.74	79.02	86.81	59.55	<b>70.91</b>	72.94	70.86	57.32	75.02
MASKOBB[43]	RX-101	89.56	85.95	54.21	72.90	76.52	74.16	85.63	89.85	83.81	86.48	54.89	69.64	73.94	69.09	63.32	75.33
CSL[34]	R-152	<b>90.25</b>	85.53	54.64	75.31	70.44	73.51	77.62	90.84	86.15	86.69	69.60	68.04	73.83	71.10	68.93	76.17
SCRDet++[44]	R-101	90.05	84.39	55.44	73.99	77.54	71.11	86.05	90.67	87.32	87.08	69.62	68.90	73.74	71.29	65.08	76.81
Single-stage:																	
DRN[45]	H-104	88.91	80.22	43.52	63.35	73.48	70.69	84.94	90.14	83.85	84.11	50.12	58.41	67.62	68.60	52.50	70.70
DAL[46]	R-101	88.61	79.69	46.27	70.37	65.89	76.10	78.53	90.84	79.98	78.41	58.71	62.02	69.23	71.32	60.65	71.78
RSDet[31]	R-101	89.90	82.90	48.60	65.20	69.50	70.10	70.20	90.50	85.60	83.40	62.50	63.90	65.60	67.20	68.00	72.20
P-RSDet[38]	R-101	88.58	77.83	50.44	69.29	71.10	75.79	78.66	90.88	80.10	81.71	57.92	63.03	66.30	69.77	63.13	72.30
RIDet-Q[36]	R-101	87.38	75.64	44.75	70.32	77.87	79.43	87.43	90.72	81.16	82.52	59.36	63.63	68.11	71.94	51.42	72.78
CFC-Net[29]	R-50	89.08	80.41	52.41	70.02	76.28	78.11	87.21	90.89	84.47	85.64	60.51	61.52	67.82	68.02	50.09	73.50
RIDet-O[36]	R-101	88.94	78.45	46.87	72.63	77.63	80.68	88.18	90.55	81.33	83.61	64.85	63.72	73.09	73.13	56.87	74.70
BBAVector[33]	R-101	88.63	84.06	52.13	69.56	78.26	80.40	88.06	90.87	87.23	86.39	56.11	65.62	67.10	72.08	63.96	75.36
R <sup>3</sup> Det[28]	R-152	89.80	83.77	48.11	66.77	78.76	83.27	87.84	90.82	85.38	85.51	65.67	62.68	67.53	78.56	72.62	76.47
PolarDet[47]	R-101	89.65	<b>87.07</b>	48.14	70.97	78.53	80.34	87.45	90.76	85.63	86.87	61.64	70.32	71.92	73.09	67.15	76.64
R3Det-DCL[35]	R-152	89.26	83.60	53.54	72.76	79.04	82.56	87.31	90.67	86.59	86.98	67.49	66.88	73.29	70.56	69.99	77.37
S <sup>2</sup> A-Net[48]	R-50	89.89	83.60	57.74	<b>81.95</b>	<b>79.94</b>	83.19	89.11	90.78	84.87	87.81	<b>70.30</b>	68.25	78.30	77.01	69.58	79.42
ROSD[49]	R-101	88.28	85.74	<b>59.79</b>	77.46	79.48	84.02	88.32	90.82	87.45	85.65	66.80	66.68	<b>78.78</b>	<b>82.52</b>	<b>74.70</b>	79.76
<b>ARP</b>	YOLOv5x	85.19	83.47	51.36	75.32	73.12	78.49	85.16	90.45	80.19	86.39	59.45	64.83	76.92	77.35	61.94	75.31
<b>ARP</b>	YOLOv5x6	85.97	83.04	52.73	76.11	75.92	79.50	88.91	90.68	79.15	<b>88.33</b>	61.20	63.28	77.29	75.83	62.94	76.05
<b>ARP+R-EIOU</b>	YOLOv5x6	88.53	83.71	53.76	80.07	77.42	82.19	84.70	90.79	86.73	87.44	64.04	63.39	76.77	80.67	66.03	77.74
<b>ARP+R-EIOU*</b>	YOLOv5x6	89.32	85.28	58.12	81.12	78.54	<b>84.11</b>	<b>89.43</b>	<b>90.91</b>	87.42	87.88	68.76	67.01	77.87	81.87	71.32	<b>79.93</b>



Figure 8: Visualization of the detection results of ARP+R-EIOU on DOTA datasets.

### 4.3.2 Results on HRSC2016

The experimental results on HRSC2016 are evaluated under PASCAL VOC2007 and VOC2012 metrics. The HRSC2016 datasets contain lots of large aspect ratios and multiple directions ship, which poses a considerable challenge for oriented object detection. As shown in Tab. 4, our method achieves 89.86% and 96.27% mAP under VOC2007 and VOC2012 metrics, respectively, outperforming most methods. Additionally, our model with YOLOv5x reaches 42 FPS on RTX 2080 Ti GPU, exceeding other detectors. More crucially, our model with YOLOv5x6 delivers state-of-the-art performance, scoring around 90.52% and 97.63% on 2007 and 2012 evaluation metrics, respectively. Fig. 9 illustrates some visualization findings on HRSC2016.



Figure 9: Detection results on HRSC2016 dataset with our method.

Table 4: Results and speed comparison on the HRSC2016 datasets.

Method	Backbone	mAP (07)	mAP (12)	FPS
R <sup>2</sup> CNN[22]	ResNet101	73.07	79.73	2
RRPN[23]	ResNet101	79.08	85.64	3.5
ROI-Transformer[27]	ResNet101	86.20	—	6
RSDet[30]	ResNet50	86.50	—	—
Gliding Vertex[32]	ResNet101	88.20	—	10
BBAVectors[33]	ResNet101	88.60	—	11.7
DAL[46]	ResNet101	88.95	—	34
R <sup>3</sup> Det[28]	ResNet101	89.26	96.01	12
R <sup>3</sup> Det-DCL[35]	ResNet101	89.46	96.41	—
CSL[34]	ResNet50	89.62	96.10	—
RIDet-O[36]	ResNet101	89.63	—	—
CFC-Net[29]	ResNet101	89.70	—	28
S <sup>2</sup> A-Net[48]	ResNet101	90.17	95.01	12.7
PolarDet[47]	ResNet50	90.46	—	25
<b>ARP+R-EIOU (ours)</b>	YOLOv5x	89.86	96.27	<b>42</b>
<b>ARP+R-EIOU (ours)</b>	YOLOv5x6	<b>90.52</b>	<b>97.63</b>	16

### 4.3.3 Results on UCAS-AOD

VOC2012 measures are used to evaluate the experimental results on USAC-AOD datasets. Our approach yields 97.04% mAP in testing, outperforming existing advanced rotation detectors such as R3Det [28] and PolarDet [47]. Furthermore, our technique has the best performance in detecting small cars, indicating that it is robust to small and densely scattered objects. The visualization results are shown in Fig. 10.

Table 5: Detection results on USAC-AOD datasets

Method	Plane	Car	mAP
YOLOv2[10]	96.60	79.20	87.90
R-DFPN[51]	95.60	82.50	89.20
DRBox[52]	94.90	85.00	89.95
S <sup>2</sup> ARN[53]	97.60	92.20	94.90
RetinaNet-H[28]	97.34	93.60	95.47
FADet[50]	98.69	92.72	95.71
R <sup>3</sup> Det[28]	98.20	94.14	96.17
RSDet[31]	98.04	94.97	96.50
SCRDet++[44]	98.93	94.97	96.95
PolarDet[47]	<b>99.08</b>	94.96	97.02
<b>ARP+R-EIOU</b>	98.91	<b>95.17</b>	<b>97.04</b>



Figure 10: Visualization of detection results on UCAS-AOD dataset with our method

#### 4.3.4 Results on ICDAR2015

We also conducted experiments on the scene text detection dataset to verify our method’s generalizability across different scenes. As illustrated in Tab. 6, our algorithm yields an 85.45% F-measure, outperforming the majority of aerial detectors and many text detectors. However, our strategy does not account for the case of a significant number of lengthy texts that are incorrectly identified as multiple short paragraphs. As a result, our system still falls short of state-of-the-art scene text identification.

Table 6: Detection results on ICDAR2015 datasets

Method	Recall	Precision	F-measure
RRPN[23]	82.17	73.23	77.44
RIL[36]	—	—	77.6
EAST[26]	78.33	83.27	80.72
TextBoxes++[24]	78.50	87.80	82.9
RSDet[31]	—	—	83.2
R <sup>2</sup> CNN[22]	79.68	85.62	82.54
DAL[46]	80.5	84.4	82.4
CSL[34]	83.00	84.30	83.65
RRD[25]	80.00	88.00	83.80
R <sup>3</sup> Det[28]	83.54	86.43	84.96
DB[54]	83.2	<b>91.8</b>	<b>87.3</b>
<b>ARP+R-EIOU</b>	<b>84.06</b>	86.28	85.16

## 5. Conclusion

In this article, we suggest a simple yet effective method for detecting orientated objects based on the area ratio of the parallelogram, which provides a unique representation of rotating objects and addresses the discontinuous boundary problem. Based on this, the area ratio of the oriented object and its smallest circumscribed rectangle was adopted to distinguish nearly horizontal objects. Additionally, R-EIOU is proposed to precisely express the loss function of rotating objects, accelerate network convergence, and enhance detection performance. Extensive experiments on multiple rotation detection datasets, including DOTA, HRSC2016, UCAS-AOD, and ICDAR2015, proved the superiority of our method.

## References

- [1] Gui-Song Xia, Xiang Bai, Jian Ding, Zhen Zhu, Serge Be-longie, Jiebo Luo, Mihai Datcu, Marcello Pelillo, and Liang-pei Zhang. DOTA: A large-scale dataset for object detection in aerial images. In CVPR, pages 3974–3983, 2018.
- [2] Zikun Liu, Liu Yuan, Lubin Weng, and Yiping Yang. A high-resolution optical satellite image dataset for ship recognition and some new baselines. In ICPRAM, pages 324–331, 2017.
- [3] Yu Li, Xian Sun, Hongqi Wang, Hao Sun, and Xiangjuan Li. Automatic target detection in high-resolution remote sensing images using a contour-based spatial model. *IEEE Geoscience and Remote Sensing Letters*, 9(5):886–890, 2012.
- [4] Junwei Han, Peicheng Zhou, Dingwen Zhang, Gong Cheng, Lei Guo, Zhenbao Liu, Shuhui Bu, and Jun Wu. Efficient, simultaneous detection of multi-class geospatial targets based on visual saliency modeling and discriminative learning of sparse coding. *ISPRS Journal of Photogrammetry and Remote Sensing*, 89:37–48, 2014.
- [5] Girshick Ross, Donahue Jeff, Darrell Trevor, and Jitendra Malik. Rich feature hierarchies for accurate object detection and semantic segmentation[C]. In Proceedings of the IEEE conference on computer vision and pattern recognition. pages 580-587, 2014.
- [6] Girshick Ross. Fast r-cnn[C]. In Proceedings of the IEEE international conference on computer vision. Pages 1440-1448, 2015.
- [7] Shaoqing Ren, Kaiming He, Ross Girshick and Jian Sun. Faster r-cnn: towards real-time object detection with region proposal networks[J]. *IEEE transactions on pattern analysis and machine intelligence*. 39(6): 1137-1149, 2016.
- [8] Kaiming He, Georgia Gkioxari, Piotr Dollár and Ross Girshick. Mask R-CNN[C]. In Proceedings of the IEEE international conference on computer vision. pages 2961-2969, 2017.
- [9] Joseph Redmon, Santosh Divvala, Ross Girshick and Ali Farhadi. You only look once: unified, real-time object detection[C]. In Proceedings of the IEEE conference on computer vision and pattern recognition, pages: 779-788, 2016.
- [10] Joseph Redmon, Ali Farhadi. Yolo9000: better, faster, stronger[C]. In Proceedings of the IEEE conference on computer vision and pattern recognition. pages 7263-7271, 2017.
- [11] Joseph Redmon, Ali Farhadi. Yolov3: An incremental improvement[J]. *arXiv preprint arXiv:1804.02767*, 2018.
- [12] Alexey Bochkovski, Chien-Yao Wang and Hong-Yuan Mark Liao. Yolov4: Optimal speed and accuracy of object detection[J]. *arXiv preprint arXiv:2004.10934*, 2020.
- [13] Wei Liu, Dragomir Anguelov, Dumitru Erhan, Christian Szegedy, Scott Reed, Chengyang Fu and Alexander C. Berg. SSD: Single shot multibox detector[C]. European conference on computer vision. Springer, Cham, pages 21-37, 2016.
- [14] Tsung-Yi Lin, Priya Goyal, Ross Girshick, Kaiming He and Piotr Dollar. Focal loss for dense object detection[C]. In Proceedings of the IEEE international conference on computer vision. Pages: 2980-2988. 2017.
- [15] Hei Law, Jia Deng. Cornernet: Detecting objects as paired keypoints[C]. In Proceedings of the European conference on computer vision. pages 734-750, 2018.
- [16] Kaiwen Duan, Song Bai, Lingxi Xie, Honggang Qi, Qingming Huang and Qi Tian. CenterNet: Keypoint triplets for object detection[C]. In Proceedings of the International Conference on Computer Vision. pages 6568–6577, 2019.
- [17] Zhaohui Zheng, Ping Wang, Wei Liu, Jinze Li, Rongguang Ye and Dongwei Ren. Distance-

- IOU loss: Faster and better learning for bounding box regression[C]. Proceedings of the AAAI Conference on Artificial Intelligence. 34(07): 12993-13000, 2020.
- [18] Jiahui Yu, Yuning Jiang, Zhangyang Wang, Zhimin Cao and Thomas Huang. Unitbox: An advanced object detection network[C]. Proceedings of the 24th ACM international conference on Multimedia. Pages 516-520, 2016.
- [19] Hamid Rezatofighi, Nathan Tsoi, JunYoung Gwak, AmirSadeghian, Ian Reid, and Silvio Savarese. Generalized intersection over union: A metric and a loss for bounding box regression. In Proceedings of the IEEE Conference on Computer Vision and Pattern Recognition, pages 658–666, 2019.
- [20] Zhaohui Zheng, Ping Wang, Wei Liu, Jinze Li, Rongguang Ye, and Dongwei Ren. Distance-IOU loss: Faster and better learning for bounding box regression. In Proceedings of the AAAI Conference on Artificial Intelligence, pages 12993–13000, 2020.
- [21] Yi-Fan Zhang, Weiqiang Ren, Zhang Zhang, Zhen Jia, Liang Wang, Tieniu Tan. Focal and efficient IOU loss for accurate bounding box regression. arXiv preprint arXiv:2101.08158, 2021.
- [22] Yingying Jiang, Xiangyu Zhu, Xiaobing Wang, Shuli Yang, Wei Li, Hua Wang, Pei Fu and Zhenbo Luo. R2cnn: rotational region cnn for orientation robust scene text detection[J]. arXiv preprint arXiv:1706.09579, 2017.
- [23] Jianqi Ma, Weiyuan Shao, Hao Ye, Li Wang, Hong Wang, Yingbin Zheng and Xiangyang Xue. Arbitrary-oriented scene text detection via rotation proposals[J]. IEEE Transactions on Multimedia, 20(11): 3111-3122, 2018.
- [24] Minghui Liao, Baoguang Shi and Xiang Bai. Textboxes++: A single-shot oriented scene text detector[J]. IEEE transactions on image processing. Pages 3676-3690, 2018.
- [25] Minghui Liao, Zhen Zhu, Baoguang Shi, Gui-song Xia and Xiang Bai. Rotation-sensitive regression for oriented scene text detection[C]. Proceedings of the IEEE conference on computer vision and pattern recognition. Pages 5909-5918, 2018.
- [26] Xinyu Zhou, Cong Yao, He Wen, Yuzhi Wang, Shuchang Zhou, Weiran He and Jiajun Liang. East: an efficient and accurate scene text detector[C]. Proceedings of the IEEE conference on Computer Vision and Pattern Recognition. Pages 5551-5560, 2017.
- [27] Jian Ding, Nan Xue, Yang Long, Gui-Song Xia and Qikai Lu. Learning roi transformer for oriented object detection in aerial images[C]. Proceedings of the IEEE/CVF Conference on Computer Vision and Pattern Recognition. Pages 2849-2858, 2019.
- [28] Xue Yang, Junchi Yan, Ziming Feng and Tao He. R3det: Refined single-stage detector with feature refinement for rotating object[C]. Proceedings of the AAAI Conference on Artificial Intelligence. Pages 3163-3171, 2021.
- [29] Qi Ming, Lingjuan Miao, Zhiqiang Zhou, Yunpeng Dong. Cfc-net: A critical feature capturing network for arbitrary-oriented object detection in remote-sensing images[J]. IEEE transactions on geoscience and remote sensing. pages:1-14, 2021
- [30] Xue Yang, Jirui Yang, Junchi Yan, Yue Zhang, Tengfei Zhang, Zhi Guo, Xian Sun and Kun Fu. Srdet: Towards more robust detection for small, cluttered and rotated objects[C]. Proceedings of the IEEE/CVF International Conference on Computer Vision. Pages 8232-8241, 2019.
- [31] Wen Qian, Wen Qian, Xue Yang, Silong Peng, Y ue Guo, and Junchi Yan. Learning modulated loss for rotated object detection. In Proceedings of the AAAI Conference on Artificial Intelligence, 2021.

- [32] Yongchao Xu, Mingtao Fu, Qimeng Wang, Yukang Wang, Kai Chen, Guisong Xia and Xiang Bai. Gliding vertex on the horizontal bounding box for multi-oriented object detection[J]. IEEE transactions on pattern analysis and machine intelligence. Pages 1452-1459, 2020.
- [33] Jingru Yi, Pengxiang Wu, Bo Liu, Qiaoying Huang, Hui Qu and Dimitris Metaxas. Oriented object detection in aerial images with box boundary-aware vectors[C]. Proceedings of the IEEE/CVF Winter Conference on Applications of Computer Vision. Pages 2150-2159, 2021.
- [34] Xue Yang, Junchi Yan. Arbitrary-oriented object detection with circular smooth label[C]. European Conference on Computer Vision. Pages 677-694, 2020.
- [35] Xue Yang, Liping Hou, Yue Zhou, Wentao Wang and Junchi Yan. Dense label encoding for boundary discontinuity free rotation detection[C]. Proceedings of the IEEE/CVF Conference on Computer Vision and Pattern Recognition. pages 15819-15829, 2021.
- [36] Qi Ming, Zhiqiang Zhou, Lingjuan Miao, Xue Yang and Yunpeng Dong. Optimization for oriented object detection via representation invariance loss[J]. arXiv preprint arXiv:2103.11636, 2021.
- [37] Xue Yang, Junchi Yan, Qi Ming, Wentao Wang, Xiaopeng Zhang and Qi Tian. Rethinking rotated object detection with gaussian wasserstein distance loss[C]. International Conference on Machine Learning, 2021.
- [38] Lin Zhou, Haoran Wei, Hao Li, Wenzhe Zhao, Yi Zhang, and Yue Zhang. Arbitrary-oriented object detection in remote sensing images based on polar coordinates. IEEE Access, 8: 223373-223384, 2020.
- [39] Haigang Zhu, Xiaogang Chen, Weiqun Dai, Kun Fu, Qixiang Ye, and Jianbin Jiao. Orientation robust object detection in aerial images using deep convolutional neural network. In 2015 IEEE International Conference on Image Processing, pages 3735–3739. IEEE, 2015.
- [40] Dimosthenis Karatzas, Lluís Gomez-Bigorda, Angelos Nicolaou, Suman Ghosh, Andrew Bagdanov, Masakazu Iwamura, Jiri Matas, Lukas Neumann, Vijay Ramaseshan Chandrasekhar, Shijian Lu, et al. Icdar 2015 competition on robust reading. In 2015 13th International Conference on Document Analysis and Recognition, pages 1156–1160. IEEE, 2015.
- [41] Seyed Majid Azimi, Eleonora Vig, Reza Bahmanyar, Marco Körner, and Peter Reinartz. Towards multi-class object detection in unconstrained remote sensing imagery. In Asian Conference on Computer Vision, pages 150–165. Springer, 2018.
- [42] Gongjie Zhang, Shijian Lu, and Wei Zhang. Cad-net: A context-aware detection network for objects in remote sensing imagery. IEEE Transactions on Geoscience and Remote Sensing, 57(12):10015 -10024, 2019.
- [43] Jinwang Wang, Jian Ding, Haowen Guo, Wensheng Cheng, Ting Pan, and Wen Yang. Mask obb: A semantic attention-based mask oriented bounding box representation for multi-category object detection in aerial images. Remote Sensing, 11(24):2930, 2019.
- [44] Xue Yang, Junchi Yan, Xiaokang Yang, Jin Tang, Wenlong Liao, and Tao He. Scrdet++: Detecting small, cluttered and rotated objects via instance-level feature denoising and rotation loss smoothing. arXiv preprint arXiv:2004.13316, 2020.
- [45] Xingjia Pan, Yuqiang Ren, Kekai Sheng, Weiming Dong, Haolei Yuan, Xiaowei Guo, Chongyang Ma, and Changsheng Xu. Dynamic refinement network for oriented and densely packed object detection. In Proceedings of the IEEE/CVF Conference on Computer Vision and Pattern Recognition, pages 11207–11216, 2020.
- [46] Qi Ming, Zhiqiang Zhou, Lingjuan Miao, Hongwei Zhang, and Linhao Li. Dynamic anchor

- learning for arbitrary-oriented object detection. In Proceedings of the AAAI Conference on Artificial Intelligence, 2020.
- [47] Pengbo Zhao, Zhenshen Qu, Yingjia Bu, Wenming Tan, Qiuyu Guan. PolarDet: a fast, more precise detector for rotated target in aerial images[J]. International Journal of Remote Sensing. pages:5831-5861, 2021.
- [48] Jiaming Han, Jian Ding, Jie Li, Gui-Song Xia. Align deep features for oriented object detection. IEEE Transactions on Geoscience and Remote Sensing, pages 1–11, 2021.
- [49] Kun Zhang, Qunqi Zeng, and Xiangyu Yu. Rosd: refined oriented staged detector for object detection in aerial image. IEEE Access, 9: 66560-66569, 2021.
- [50] Chengzheng Li, Chunyan Xu, Zhen Cui, Dan Wang, Tong Zhang, and Jian Yang. Feature-attended object detection in remote sensing imagery. In 2019 IEEE International Conference on Image Processing, pages 3886–3890, 2019.
- [51] Xue Yang, Hao Sun, Kun Fu, Jirui Yang, Xian Sun, Meng long Yan, and Zhi Guo. Automatic ship detection in remote sensing images from google earth of complex scenes based on multi-scale rotation dense feature pyramid networks. Remote Sensing, 10(1):132, 2018
- [52] Lei Liu, Zongxu Pan, and Bin Lei. Learning a rotation invariant detector with rotatable bounding box. arXiv preprint arXiv:1711.09405, 2017.
- [53] Songze Bao, Xing Zhong, Ruifei Zhu, Xiaonan Zhang, Zhuqiang Li, and Mengyang Li. Single shot anchor refinement network for oriented object detection in optical remote sensing imagery. IEEE Access, 7:87150–87161, 2019.
- [54] Minghui Liao, Zhaoyi Wan, Cong Yao, Kai Chen, and Xiang Bai. Real-time scene text detection with differentiable binarization. In Proceedings of the AAAI Conference on Artificial Intelligence, pages 11474–11481, 2020.